electronics

MDPI

Article

Behavior of 3D Printed Stretchable Structured Sensors

Eugene Kim [1], Seyedmeysam Khaleghian [2] and Anahita Emami [3,*]

[1] Department of Mechanical Engineering, University of Texas at Dallas, Dallas, TX 75080, USA
[2] Department of Engineering Technology, Texas State University, San Marcos, TX 78666, USA
[3] Ingram School of Engineering, Texas State University, San Marcos, TX 78666, USA
* Correspondence: a.emami@txstate.edu

Abstract: Piezoresistive structures inspired by serpentines, auxetic, and kirigami arrangements have demonstrated good flexibility and sensitivity under tension. Piezoresistive structures display optimal performance when the characteristics entail reliable stretchability and repeatability. These structures can be implemented as wearable sensors by compressing and elongating the conductive nanocomposites to vary the flow of electrons and to provide resistance change. To guarantee the reliability of these structures for strain sensing, it is important that the resistance change in these structures remains constant under repeated loads. In this study, the performance of different piezoresistive structures under cyclic tensile load is investigated and compared. Based on the performance of different types of structures, novel hybrid structures have been also proposed to design for both high stretchability and sensitivity of piezoresistive sensors. All the structures were tested with position limits rather than a fixed force to avoid permanent deformation. First, small position limits were used to determine Young's Modulus, then a 10-cycle tensile test with larger position limits was used to further study the electromechanical behavior of different piezoresistive structures under larger deformation and repetition. Finally, the gage factor was derived for all the studied structures, and they were re-categorized based on properties' similarities.

Keywords: serpentine; auxetic; kirigami; gauge factor; piezoresistive

check for updates

Citation: Kim, E.; Khaleghian, S.; Emami, A. Behavior of 3D Printed Stretchable Structured Sensors. *Electronics* **2023**, *12*, 18. https://doi.org/10.3390/electronics12010018

Academic Editors: Piero Cosseddu and Mengfang Li

Received: 1 December 2022
Revised: 15 December 2022
Accepted: 17 December 2022
Published: 21 December 2022

1. Introduction

Flexible piezoresistive sensors are commonly used in different applications such as healthcare, wearable devices [1–3], prosthetics [4,5], human physiological activity monitoring [6], and rehabilitation devices [7], as well as advanced technologies such as soft robotics [8,9] and human–machine interfaces [10]. The advancement in additive manufacturing of piezoresistive composite materials [11–14] offers design freedom for architected sensors. Despite the abundant applications of flexible architected sensors, few studies have been thoroughly conducted around the idea of optimal structures capable of measuring large elongation with high sensitivity. Investigating the electromechanical behavior of different structures and categorizing them based on their gauge factors will provide useful insights into the design of architected sensors. Moreover, having lower stress concentrations to prevent failure due to large elongation is important for improving the durability of the piezoresistive structure in large strain measurement applications. Although the choice of material assists with preventing permanent deformation and damage, designing a structure with better fluidity in motion helps alleviate rigid behavior and allows for greater resistance change. With a combination of different structures, such as auxetic, kirigami, and serpentine structures, a variety of structures can be designed to test the behavior and properties of each structure.

According to Widlund et al. [15], the stretchability of the serpentine structure depends on the arc angle, which is the amount of curvature the serpentine structure rotates. Testing the arc angle with a ratio of maximum and applied strain, this research concluded that serpentine structures greater than an arc angle of 180 degrees are optimally stretchable.

Therefore, this concept was used to create novel hybrid structures that implement this concept for greater stretchability. The stretchability is also greater when embedding electromechanical nanocomposites into a pre-strained elastomer [16]. This method would be significant for the structures introduced within this paper, since it would provide a pre-load and enhance the stretchability for greater resistance change. Moreover, the use of the elastomer creates the opportunity for biaxial structures with a Poisson's ratio of close to 0.5 to elongate further.

Although Poisson's Ratio is not the main focus of this research, using auxetic structures changes the effect of strain sensors. Comparing re-entrant and S-shaped structure with finite element analysis, the S-shape structure was capable of maintaining better conditions under compression [17]. Allowing sharp edges to be revised with larger curvature decreased stress concentrations. Using similar structures, the entire test could be transferred into being tested in tension with sensor material.

The re-entrant auxetic structure is not very stretchable, so Jiang et al. [18] decided to run a test of 2300 cycles to understand the properties of the auxetic structure after repetitive use, such as microcracking and gauge factor. The smaller the Poisson's ratio, the larger the gauge factor determined. Using a scanning electron microscope (SEM), the microcracking was seen to be long instead of short like a flat rectangular structure.

Kirigami structures of soft material portray out-of-plane bending. Zhou et al. [19] was capable of removing the out-of-plane bending by adding thin linkages. The linkages were also capable of supporting greater stretchability. Lee et al. [20] developed kirigami sensors with patterned mesh designs which showed low change in resistance, 0.23%, when the strain met 100%, meaning that the gauge factor was 0.23. The main issue with kirigami structures for tensile sensors is that the sensitivity is very low, since kirigami structures rely heavily on a pre-load before any deformation. Moreover, the thin linkages within kirigami structures typically experience lower deformation, since slits or cuts are made into a rigid body, which is not easily stretched. Kirigami structures are mainly useful for non-malleable material, such as metal; however, when the concept is implemented into elastic material, the stretchability significantly increases.

When using cyclic tensile loading with small loads, the kirigami structures are not very responsive. Two kirigami-related structures were tested under cyclic loading and the percent change of gauge factor turned out to be -95 and -90 [21]. When further inspecting the resistance versus strain plot, the change in resistance almost resembled a constant function, while all other tested structures provided large resistance change. This shows that although the structure contains less stress concentrations and greater stretchability, the structural integrity is not capable of undergoing deformation to re-orient conductive filler particles.

In this study, three different categories of structures were studied, including a re-entrant auxetic structure, three kirgami-based structures, and three serpentine-based structures. To the best of authors' knowledge, this is the first study to focus on evaluating the performance of these three categories of structures for sensor applications comparatively under the same cyclic loading conditions. In addition, modified and novel designs of serpentine-based, kirgami-based, and hybrid kirigami-serpentine-based structures have been proposed and studied for the first time in this work. Moreover, a negative gauge factor has been observed in all these 3D printed structures, which will be discussed further in the Discussions section.

In this work, first, the re-entrant auxetic structure will be tested and its performance will be compared with other structures, since it is one of the most widely used auxetic structures for different applications, including strain sensors [22,23]. Out of most variations of auxetic structures, the re-entrant demonstrated superior performance for strain-sensing applications [23]. Therefore, this type of structure will be further investigated in this study and will compared with more stretchable structures. The serpentine structures will be also studied, since they are capable of elongating to large percentages, especially with an arc angle greater than 180 degrees [15]. Moreover, serpentine structures with sharp corners have large stress concentrations, resulting in higher sensitivity, which will be studied and compared with other serpentine structures [17]. Finally, a kirigami structure introduced by Zhou et al. [19], which is capable of elongating as a thin structure without losing sensor properties, will also be considered in this study. The design of this structure will be also modified to enhance the sensor sensitivity and durability.

2. Methodology

For the seven structures, there was a general three-step process: design and finite element analysis, 3D printing, and experimental tensile tests. The structures were designed based on inspiration and previously mentioned structures. Seven different structures were used in this study, including six widely used structures and an inspire-designed one. The selected structures include Curved Re-Entrant (CRE), Kirigami Dumbbell (KD), Kirigami H-Shape (KHS), Kirigami Hybrid (KH), Serpentine Shape (SS), Reduced Curve Serpentine Shape (RCSS), and Hourglass-Inspired Serpentine Shape (HISS). As demonstrated in Figure 1, CRE, RCSS, SS, and KHS are also slightly modified, compared to their original design, and the original design was used for the other three structures. The designs of both KD and KH are inspired by KHS. The KD structure has more curvature and less materials, which makes it more flexible compared to KHS. The KH structure is not only made of less materials but also uses a serpentine shape link instead of a straight link, which makes it much more stretchable than KD and KHS.

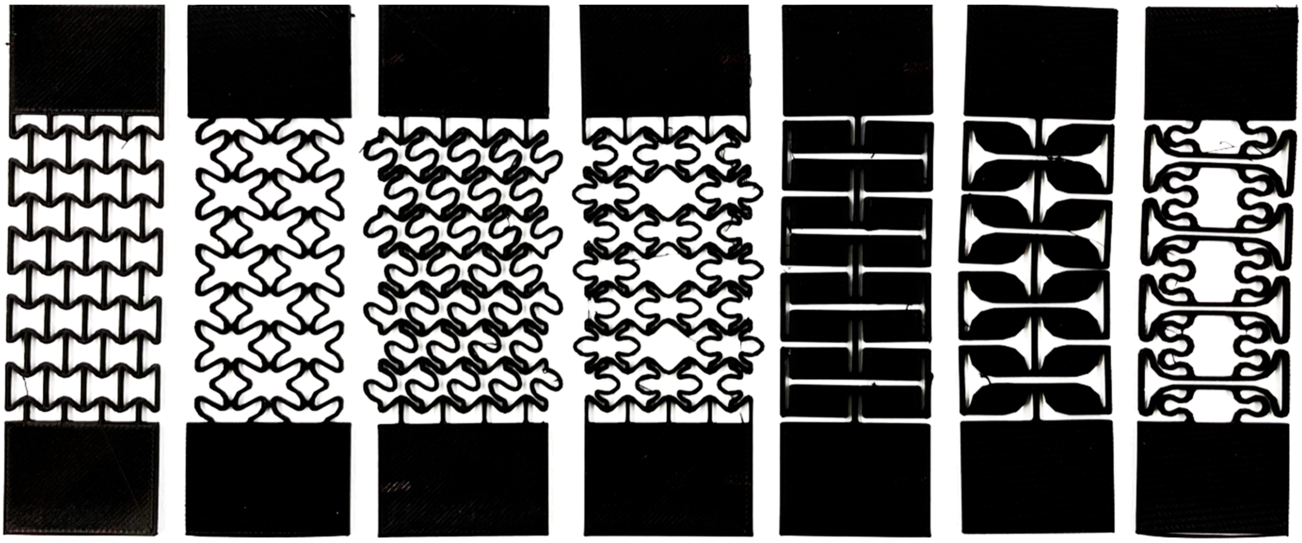

Figure 1. The printed samples, left to right: CRE, RCSS, SS, HISS, KHS, KD, and KH.

The dimension of each structure was designed as 60 mm × 30 mm × 1.5 mm, respectively, in length, width, and height. The connecting link width was set at 0.975 mm for the KHS, KD, and KH samples, and 0.75 mm for the CRE, RCSS, SS, and HISS ones. An additional 15 mm of uniform rectangles was added at each end of all structures in order to ensure uniform distribution loading conditions during the tensile tests.

All the selected structures were then modeled in SolidWorks, and their performance, especially their deformation and stress concentration, was evaluated under the simulated tensile test. Eel 3D Printing Filament by NinjaTek, which contains 18% carbon black, 0.3% silica and cristobalite, and 82% thermoplastic polyurethane (TPU) resin, was used to print all the structures. Based on the product data sheet, this filament can endure elongation of up to 355% repeatedly without damage. Due to biocompatibility and biodegradability of TPU, it is very desirable for wearables and biomedical applications. Adding various conductive nanoparticles make this polymer a good candidate for flexible sensors. However, polymeric nanocomposites also have some disadvantages, such as non-linear mechanical behavior along with viscoelastic and hysteresis effect under cyclic loading. Moreover, TPU nanocomposite filament is also hygroscopic and absorbs moisture from the air, which can affect its electromechanical properties. Therefore, PrintDry Pro was used as the de-humidifier (shown in Figure 2b), and the filament was kept in the de-humidifier during the course of this study to prevent the effect of moisture on the conductivity and mechanical properties of the filament.

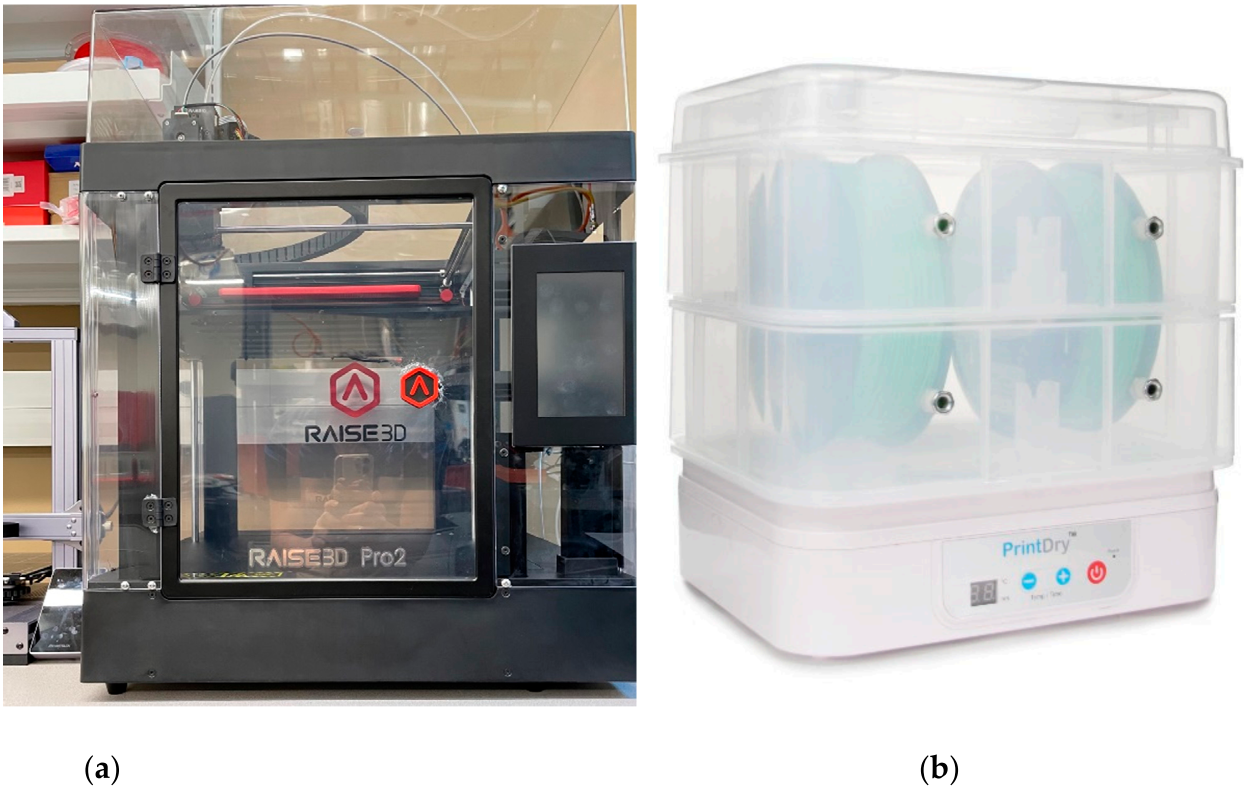

Figure 2. (**a**) Raise3D Pro2 3D printer was used to fabricate all structures. (**b**) PrintDry Pro was used to prevent moisture in structures.

The method of printing in this study for all the structures is Fused Deposition Modeling (FDM) since it is most compatible with printing highly conductive designs. Raise3D Pro2 printer by Raise3D, shown in Figure 2a, was used in this study. The original printing setting of the 3D printer was used, and the infill was set to 100% to maximize the conductive contact points. The printed samples are shown in Figure 1.

ADMET eXpert 7600, which is a single-column universal testing machine, was used for the tensile testing. The universal testing machine is shown in Figure 3 The time-synchronized data of force, displacement, and the voltage from the printed sensors are logged through a USB NI-DAQ along with a data-collecting routine, developed in LabVIEW. The DAQ has a resistor and needed to be adjusted to fit the resistance of the structures.

The initial resistances of all seven structures, as shown in Table 1, were measured with a multimeter, which concluded by using a 10 KΩ resistor to benefit all structures. The input voltage was 5.00 volts for all seven structures; the measured resistances are presented in Table 1.

The structures were individually tested with a simple one-cycle tensile test and a cyclic tensile test. The cyclic tensile test was conducted to study the electromechanical behavior of different structures. Since the amount of load the structures could withstand was unknown, the position limits were adjusted for each structure separately in the tensile test. The testing parameters used for different structures are shown in Table 2.

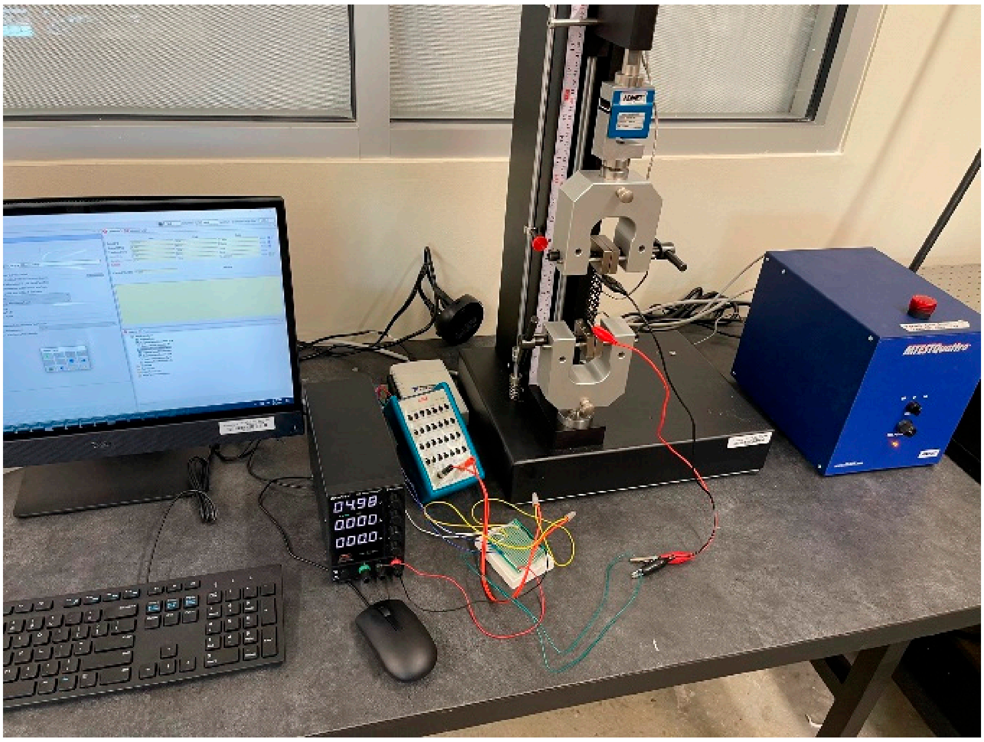

Figure 3. Tensile test machine used in the experiments.

Table 1. Initial measured resistance of structure.

Name	Resistance (kΩ)
Curved Re-Entrant (CRE)	10.84
Reduced Curve Serpentine Shape (RCSS)	17.12
Serpentine Shape (SS)	15.41
Hourglass Inspired Serpentine Shape (HISS)	19.52
Kirigami H-Shape (KHS)	34.94
Kirigami Dumbbell (KD)	36.64
Kirigami Hybrid (KH)	45.9

Table 2. Tensile testing parameters for each structure, where lower position limit, gripper displacement rate, and sample rate are constant throughout the entire testing process.

Name	Lower Position Limit (mm)	Upper Cyclic Position Limit (mm)	Gripper Displacement Rate (mm/min)	Sample Rate (sample/s)
CRE	0.00	10.00	300.00	100.00
RCSS	0.00	15.00	300.00	100.00
SS	0.00	15.00	300.00	100.00
HISS	0.00	15.00	300.00	100.00
KHS	0.00	30.00	300.00	100.00
KD	0.00	30.00	300.00	100.00
KH	0.00	60.00	300.00	100.00

The structures were carefully aligned vertically and were appropriately fixed by the gripper in the universal testing machine, as shown in Figure 4. The gripper was clipped at the center of the blank canvas on the end of structures, which is 7.5 mm away from the edge, then uniaxially loaded.

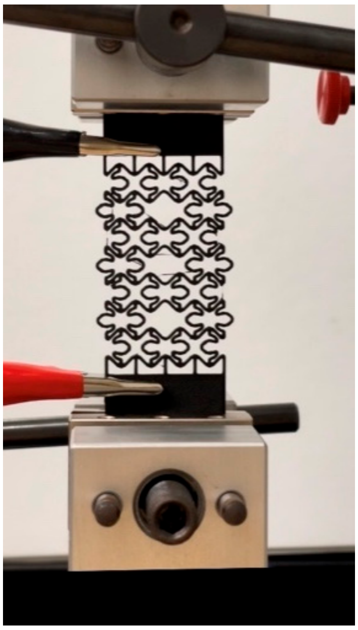

Figure 4. Image of structure for tensile test.

A small pre-load was applied on the kirigami structures to compensate for the initial rigid body motion (rotation of inclined linkages). Since the amount of load each structure could withstand was unknown, a small pre-load of 0.05 N was used in all structures. Alligator clips were directly attached to both ends of printed structures, as shown in Figure 4.

Then, the gauge factor (GF) was derived from the resistance vs. strain graph as follows:

$$\mathrm{GF} = (\Delta \mathrm{R}/\mathrm{R})/\varepsilon \tag{1}$$

where R is resistance and ε is the strain.

3. Results

The Finite Element Analysis (FEA) of all seven structures and their corresponding performance under experimental tensile testing are shown in Figures 5–11. The FEA was mainly used to identify the connections with the highest stress concentrations in different structures, in order to remove or alleviate them, and also to determine the structures' stretchability performance under constant loading. The FEA is used to understand how different structures deform under tensile load and if the material yields at critical points where the maximum stress concentration is observed.

The experimental results for all seven structures are presented in Figures 12–18, and in each figure, there are four plots for each structure representing the cyclic load test. The first and last cycle are isolated to show the change in resistance over repetitive strain. As demonstrated in Figure 6, the CRE has low elongation range due to the structural resistance to deformation. On the other hand, the kirigami structures (KHS, KD, and KH) have large elongation ranges, which are shown in Figures 16–18. The serpentine structures, RCSS, SS, and HISS, have larger elongation ranges than CRE, but not significantly so. Next, the gauge factor can be determined by calculating the slope of the resistance versus strain graph.

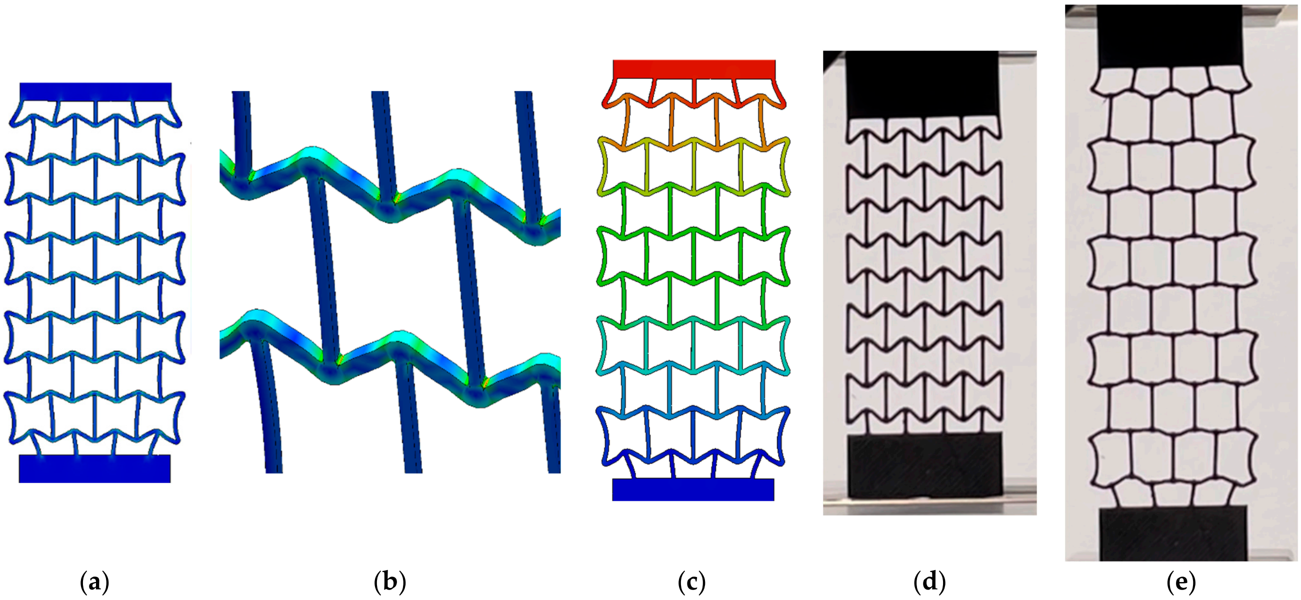

Figure 5. CRE structure with FEA, unstretched length, and stretched length: (**a**) FEA stress analysis, (**b**) FEA close-up for stress concentration, (**c**) FEA displacement, (**d**) printed structure, (**e**) stretched printed structure.

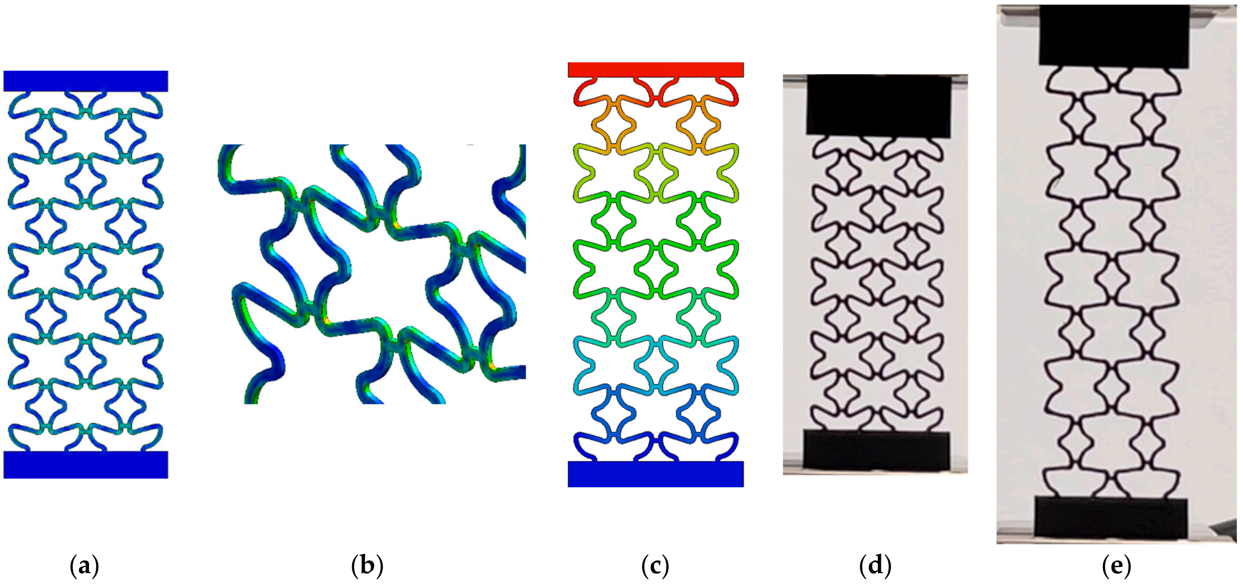

Figure 6. RCSS structure with FEA, unstretched length, and stretched length: (**a**) FEA stress analysis, (**b**) FEA close-up for stress concentration, (**c**) FEA displacement, (**d**) printed structure, (**e**) stretched printed structure.

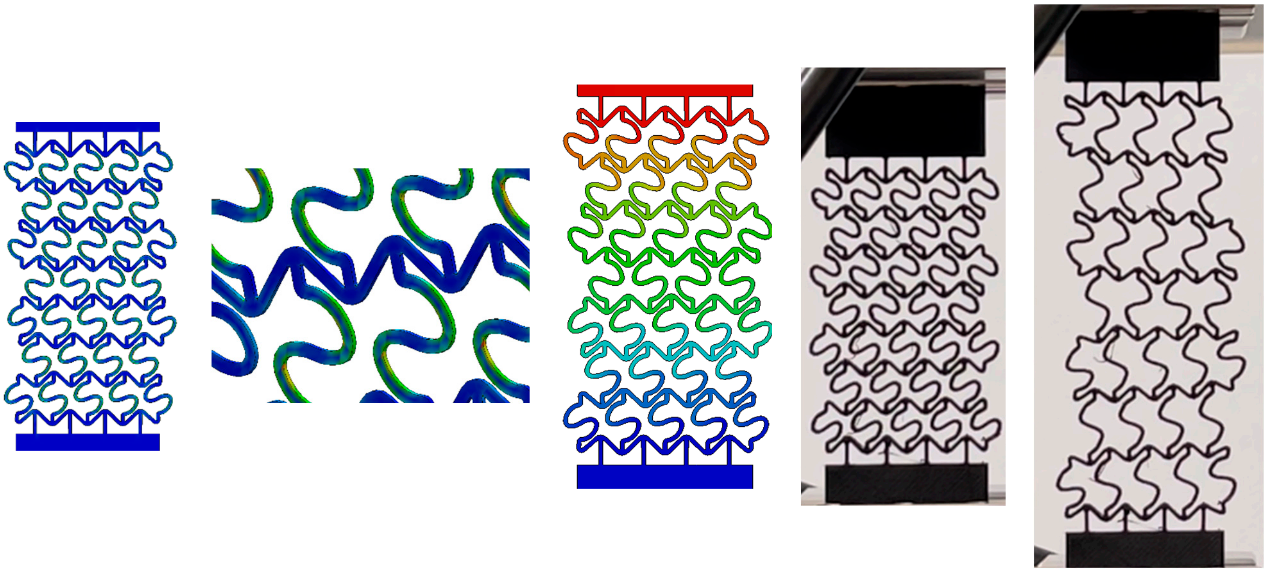
(**a**) (**b**) (**c**) (**d**) (**e**)

Figure 7. SS structure with FEA, unstretched length, and stretched length: (**a**) FEA stress analysis, (**b**) FEA close-up for stress concentration, (**c**) FEA displacement, (**d**) printed structure, (**e**) stretched printed structure.

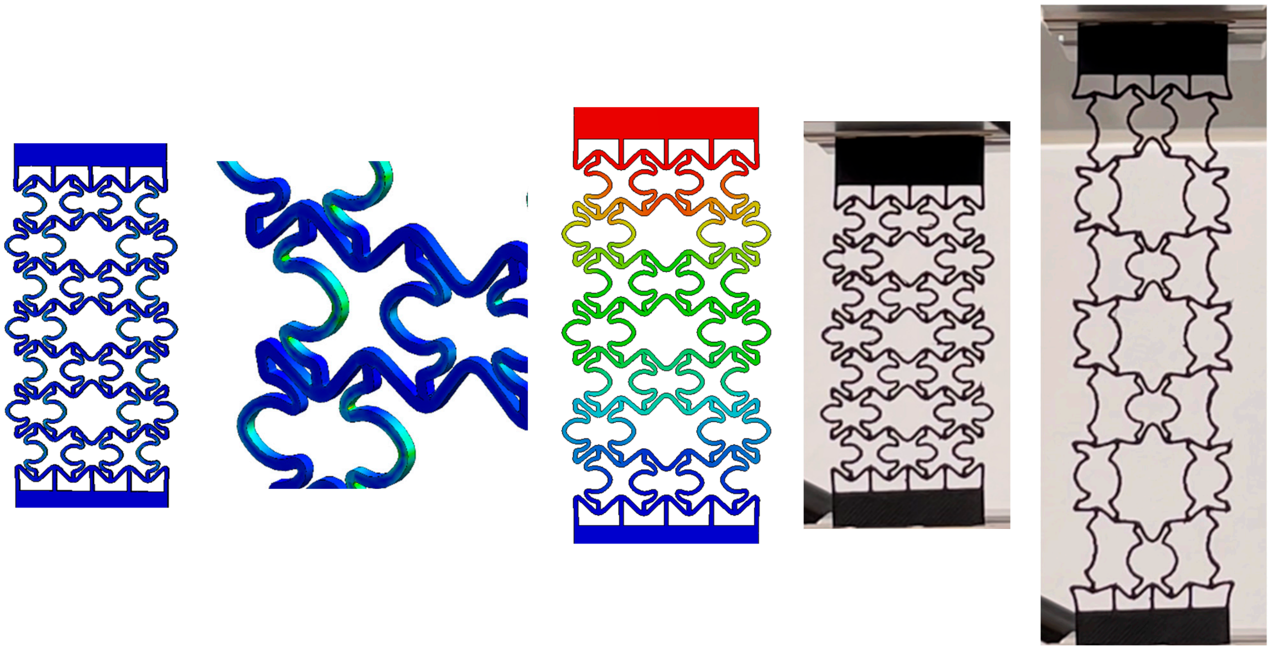
(**a**) (**b**) (**c**) (**d**) (**e**)

Figure 8. HISS structure with FEA, unstretched length, and stretched length: (**a**) FEA stress analysis, (**b**) FEA close-up for stress concentration, (**c**) FEA displacement, (**d**) printed structure, (**e**) stretched printed structure.

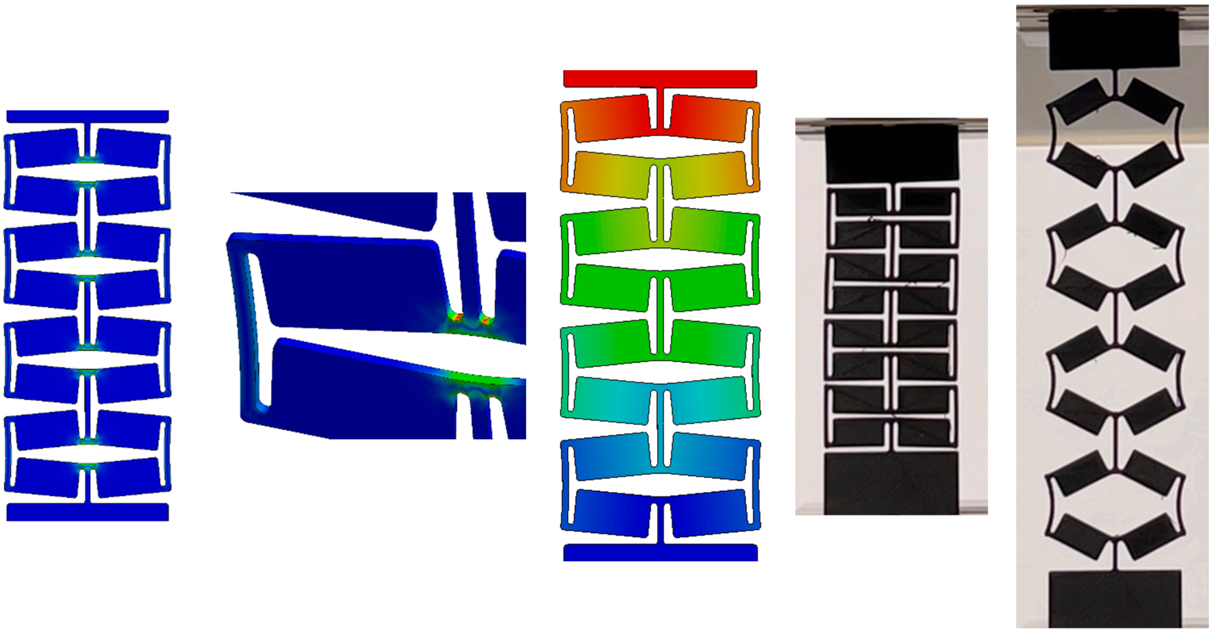

(**a**) (**b**) (**c**) (**d**) (**e**)

Figure 9. KHS structure with FEA, unstretched length, and stretched length: (**a**) FEA stress analysis, (**b**) FEA close-up for stress concentration, (**c**) FEA displacement, (**d**) printed structure, (**e**) stretched printed structure.

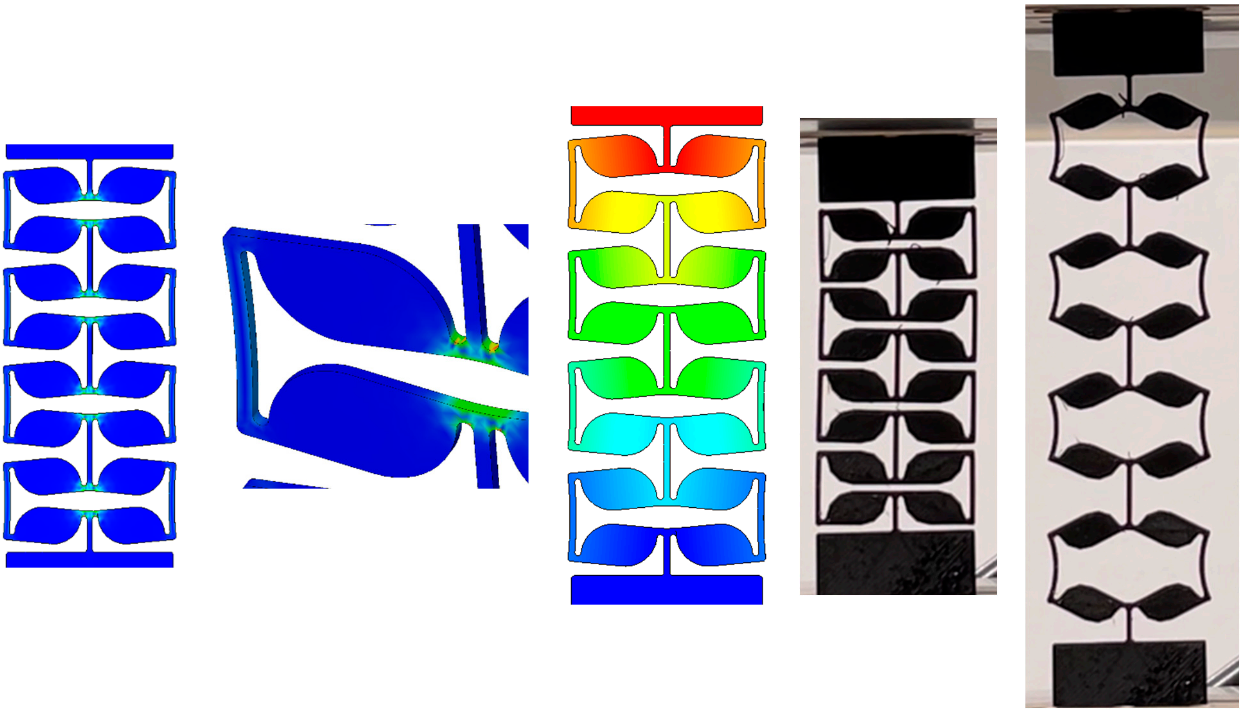

(**a**) (**b**) (**c**) (**d**) (**e**)

Figure 10. KD structure with FEA, unstretched length, and stretched length: (**a**) FEA stress analysis, (**b**) FEA close-up for stress concentration, (**c**) FEA displacement, (**d**) printed structure, (**e**) stretched printed structure.

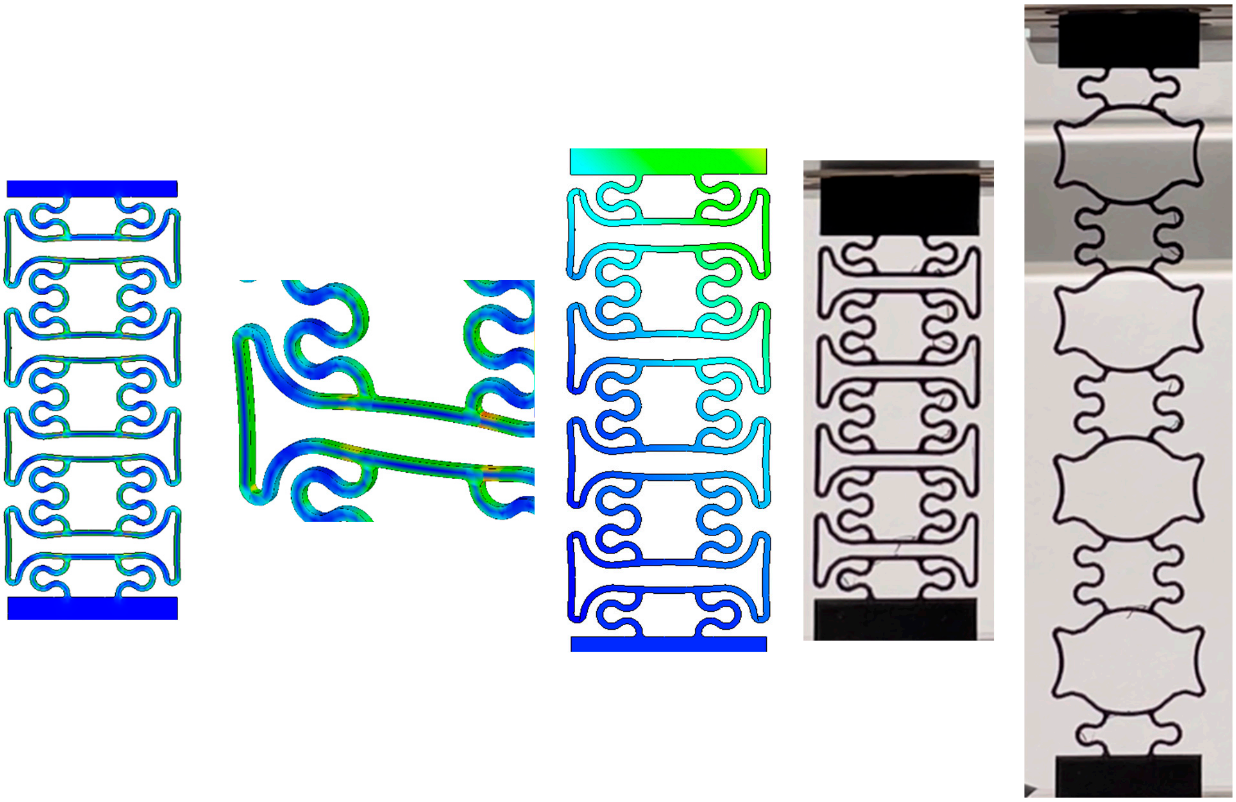

(**a**) (**b**) (**c**) (**d**) (**e**)

Figure 11. KH structure with FEA, unstretched length, and stretched length: (**a**) FEA stress analysis, (**b**) FEA close-up for stress concentration, (**c**) FEA displacement, (**d**) printed structure, (**e**) stretched printed structure.

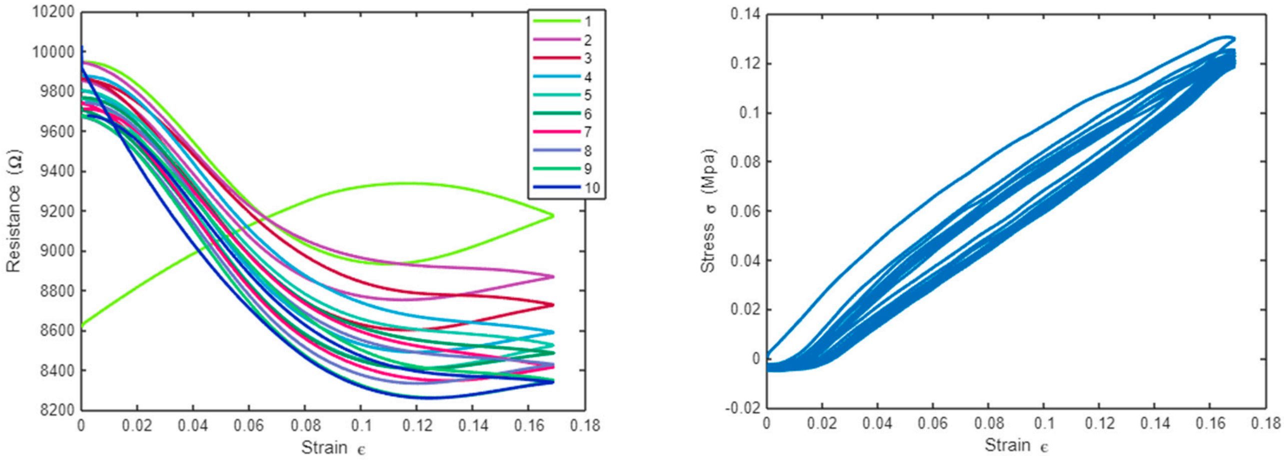

(**a**) (**b**)

Figure 12. *Cont.*

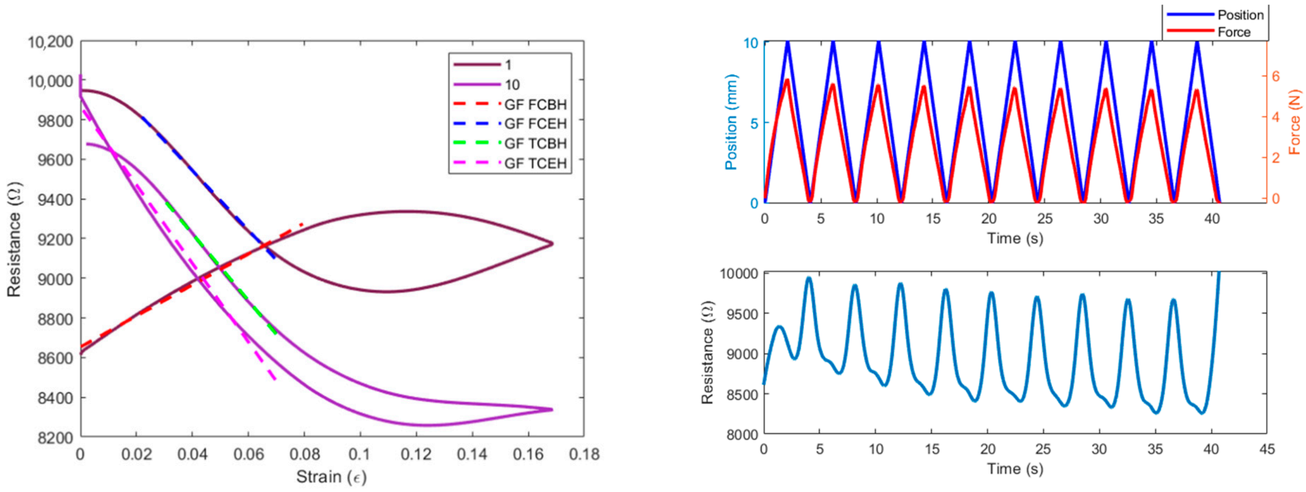

(**c**) (**d**)

Figure 12. CRE cyclic tensile test results: (**a**) Resistance vs. strain for ten cycles. (**b**) Stress vs. strain for ten cycles. (**c**) Resistance vs. strain and gauge factors for the first and the tenth cycles. (**d**) Displacement, force, and resistance change over time for ten cycles.

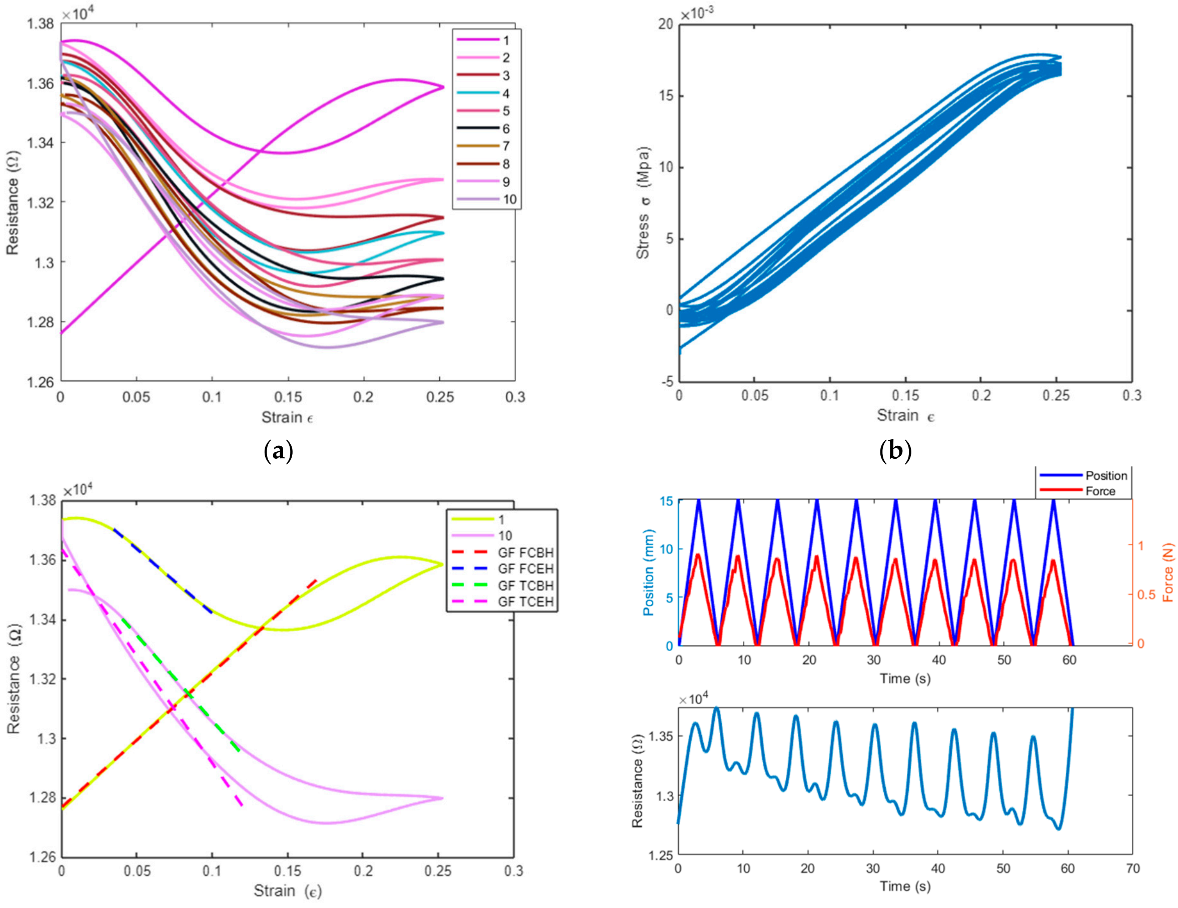

(**a**) (**b**)

(**c**) (**d**)

Figure 13. RCSS cyclic tensile test results: (**a**) Resistance vs. strain for ten cycles. (**b**) Stress vs. strain for ten cycles. (**c**) Resistance vs. strain and gauge factors for the first and the tenth cycles. (**d**) Displacement, force, and resistance change over time for ten cycles.

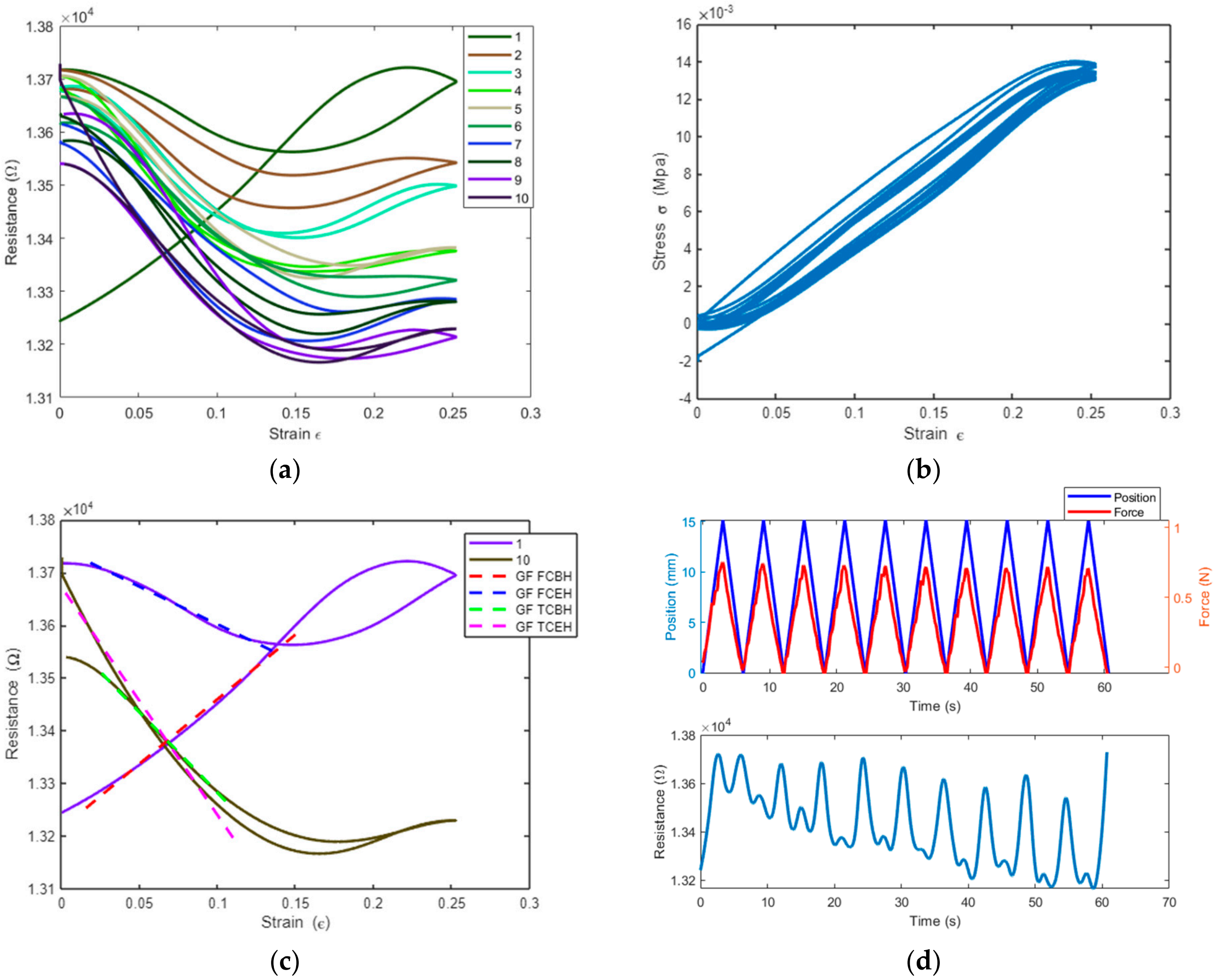

Figure 14. SS cyclic tensile test results: (**a**) Resistance vs. strain for ten cycles. (**b**) Stress vs. strain for ten cycles. (**c**) Resistance vs. strain and gauge factors for the first and the tenth cycles. (**d**) Displacement, force, and resistance change over time for ten cycles.

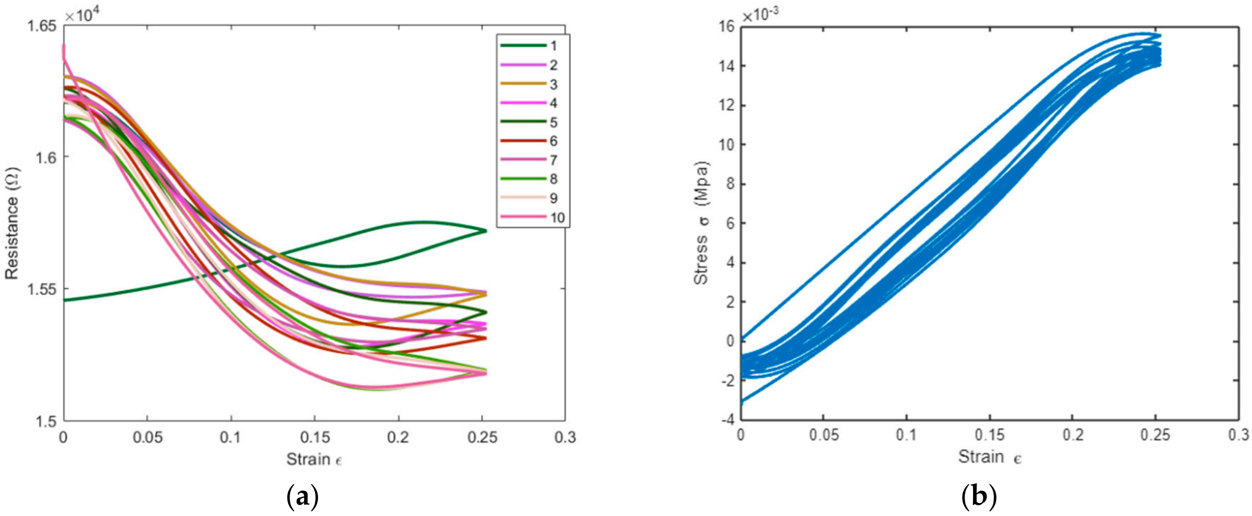

Figure 15. *Cont.*

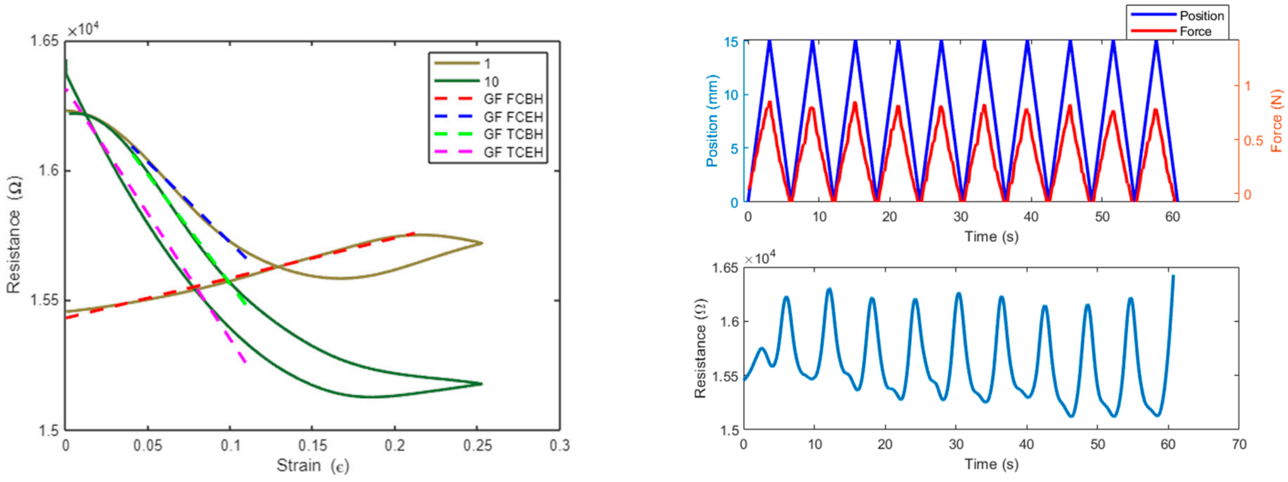

(**c**) (**d**)

Figure 15. HISS cyclic tensile test results: (**a**) Resistance vs. strain for ten cycles. (**b**) Stress vs. strain for ten cycles. (**c**) Resistance vs. strain and gauge factors for the first and the tenth cycles. (**d**) Displacement, force, and resistance change over time for ten cycles.

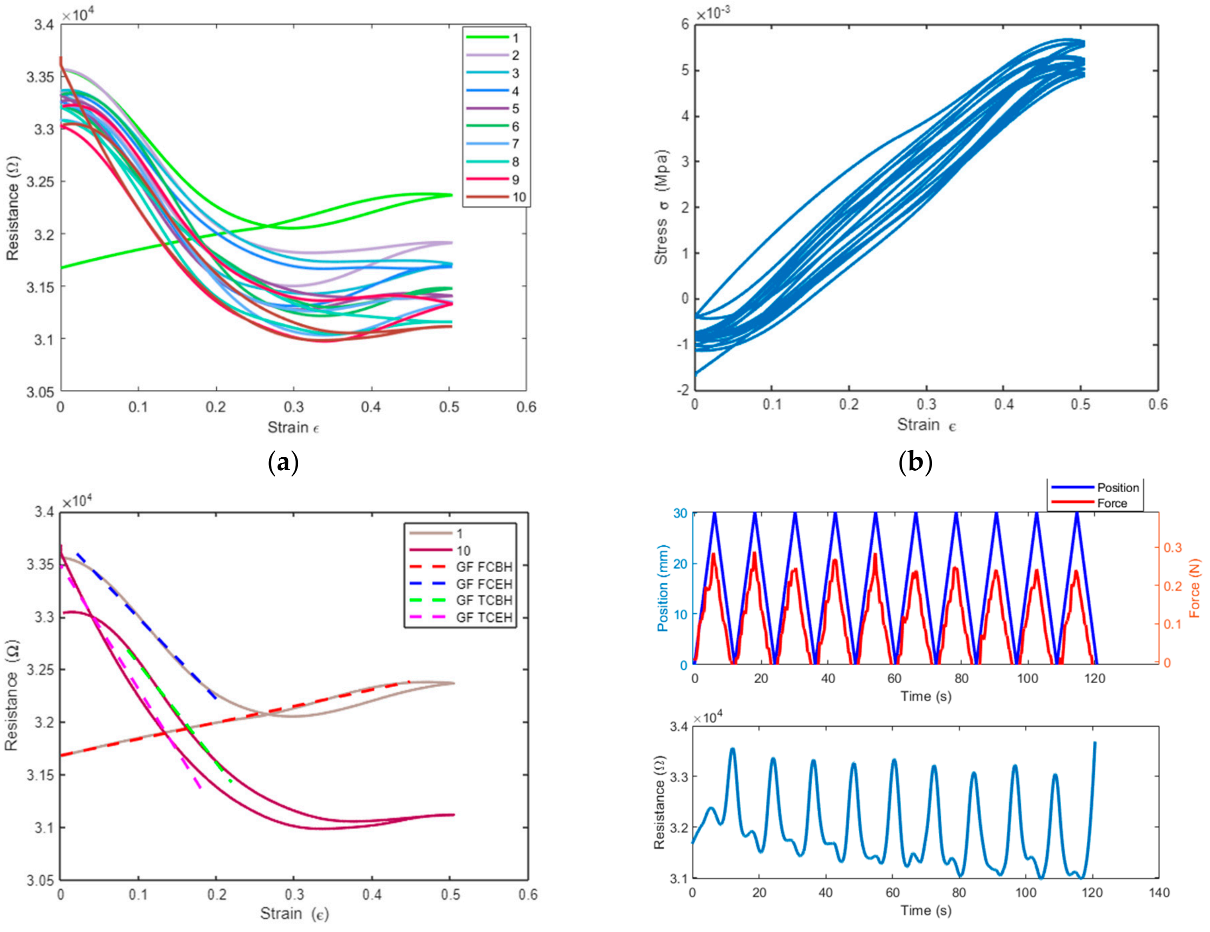

(**a**) (**b**)

(**c**) (**d**)

Figure 16. KHS cyclic tensile test results: (**a**) Resistance vs. strain for ten cycles. (**b**) Stress vs. strain for ten cycles. (**c**) Resistance vs. strain and gauge factors for the first and the tenth cycles. (**d**) Displacement, force, and resistance change over time for ten cycles.

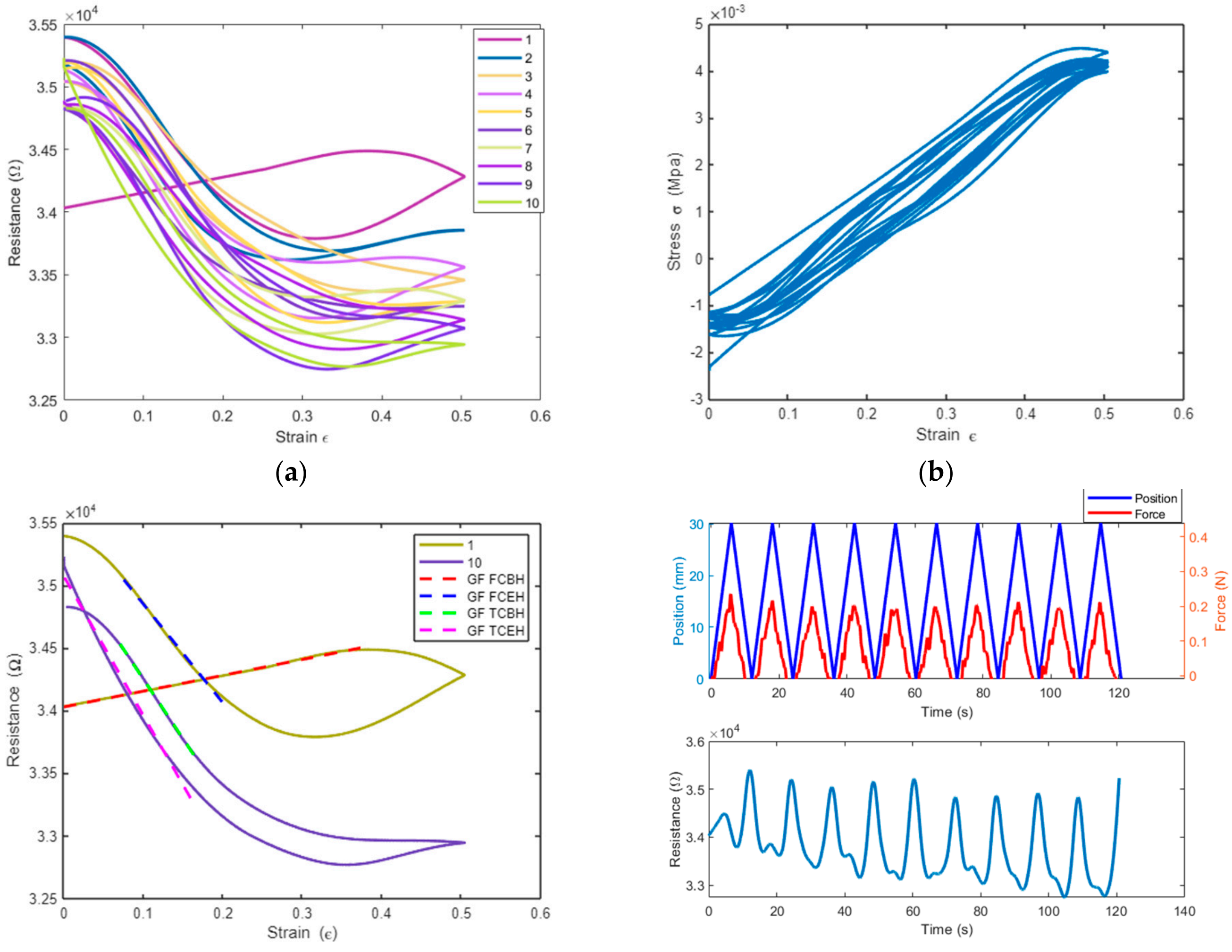

(**a**) (**b**)

(**c**) (**d**)

Figure 17. KD cyclic tensile test results: (**a**) Resistance vs. strain for ten cycles. (**b**) Stress vs. strain for ten cycles. (**c**) Resistance vs. strain and gauge factors for the first and the tenth cycles. (**d**) Displacement, force, and resistance change over time for ten cycles.

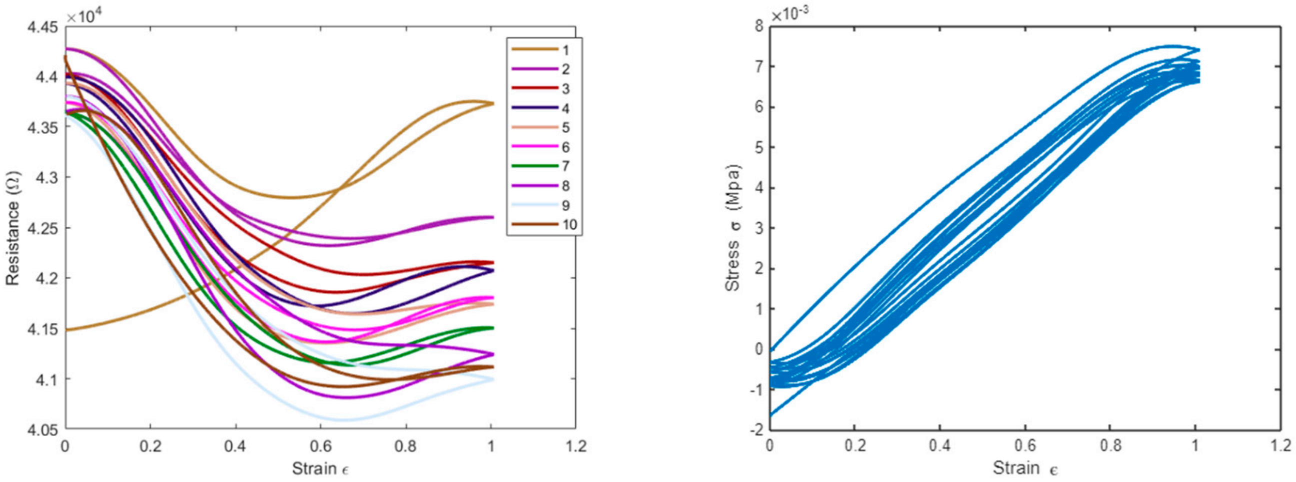

(**a**) (**b**)

Figure 18. *Cont.*

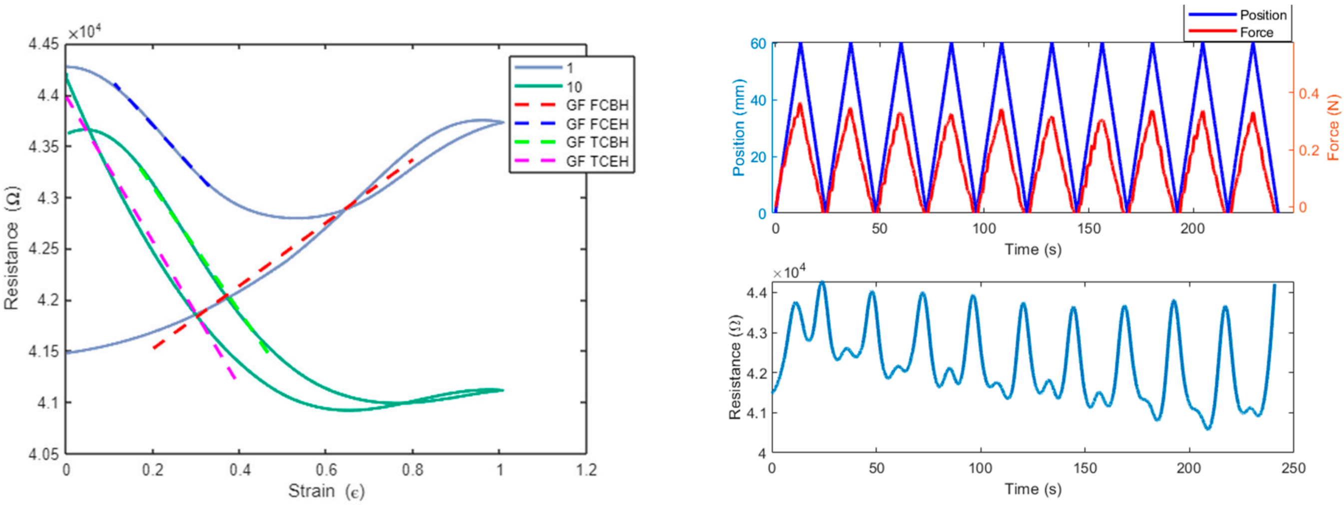

(**c**) (**d**)

Figure 18. KH cyclic tensile test results: (**a**) Resistance vs. strain for ten cycles. (**b**) Stress vs. strain for ten cycles. (**c**) Resistance vs. strain and gauge factors for the first and the tenth cycles. (**d**) Displacement, force, and resistance change over time for ten cycles.

The change of resistance by strain, and the initial resistance for all the seven structures is presented in Figures 19 and 20, respectively. These values were utilized to calculate the gauge factor for different structures using Equation (1), which is presented in Figure 21.

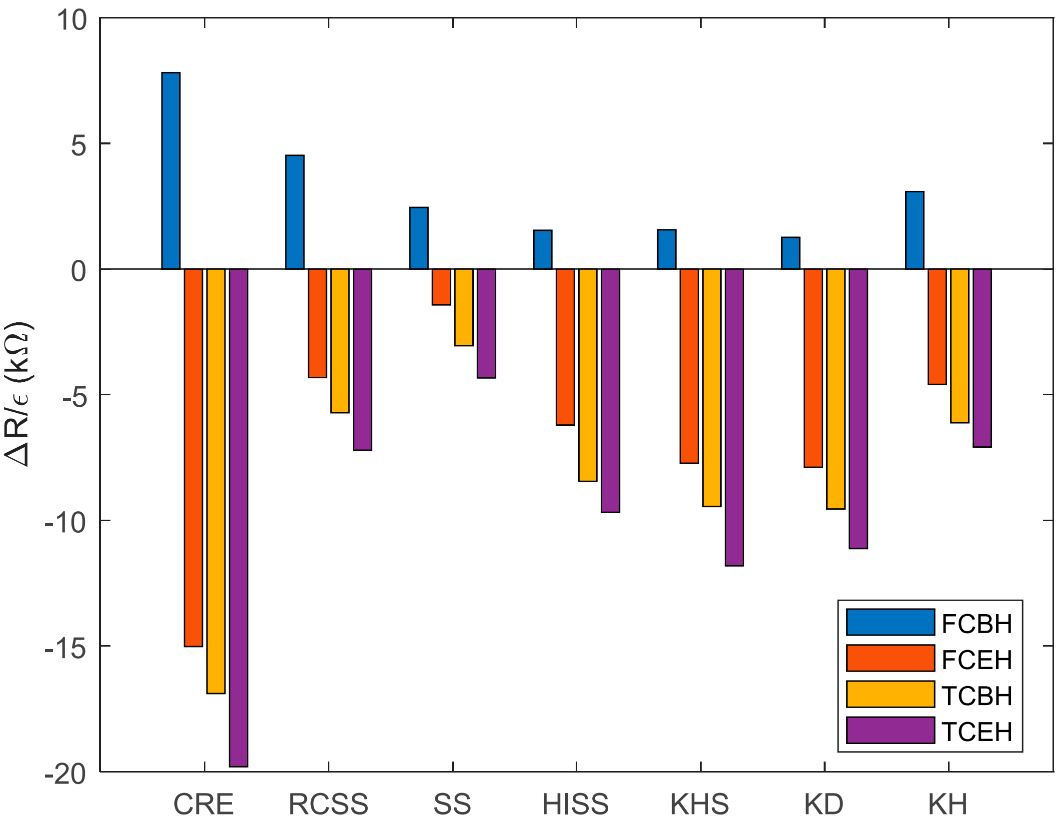

Figure 19. Values of resistance change over strain are provided for each structure. FCBH: first cycle before halfway; FCEH: first cycle end of halfway; TCBH: tenth cycle before halfway; TCEH: tenth cycle end of halfway.

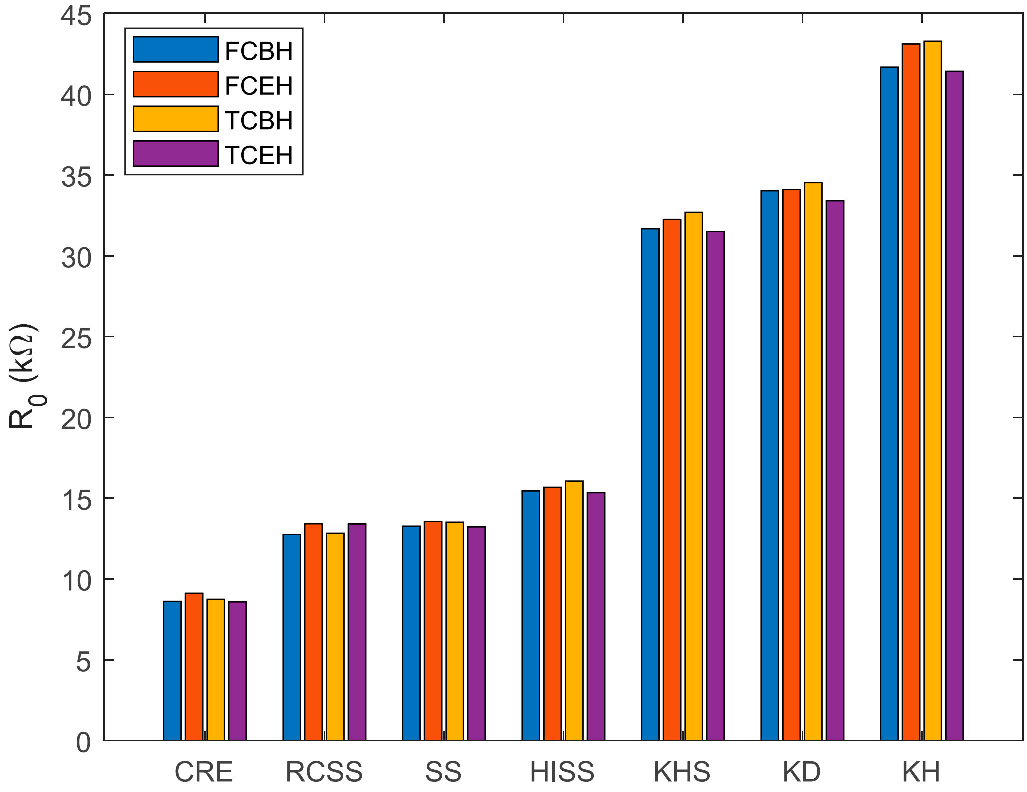

Figure 20. Initial resistance found by pinpointing direction of the cycle within the resistance vs. strain graph and noting the proper value before deriving the slope.

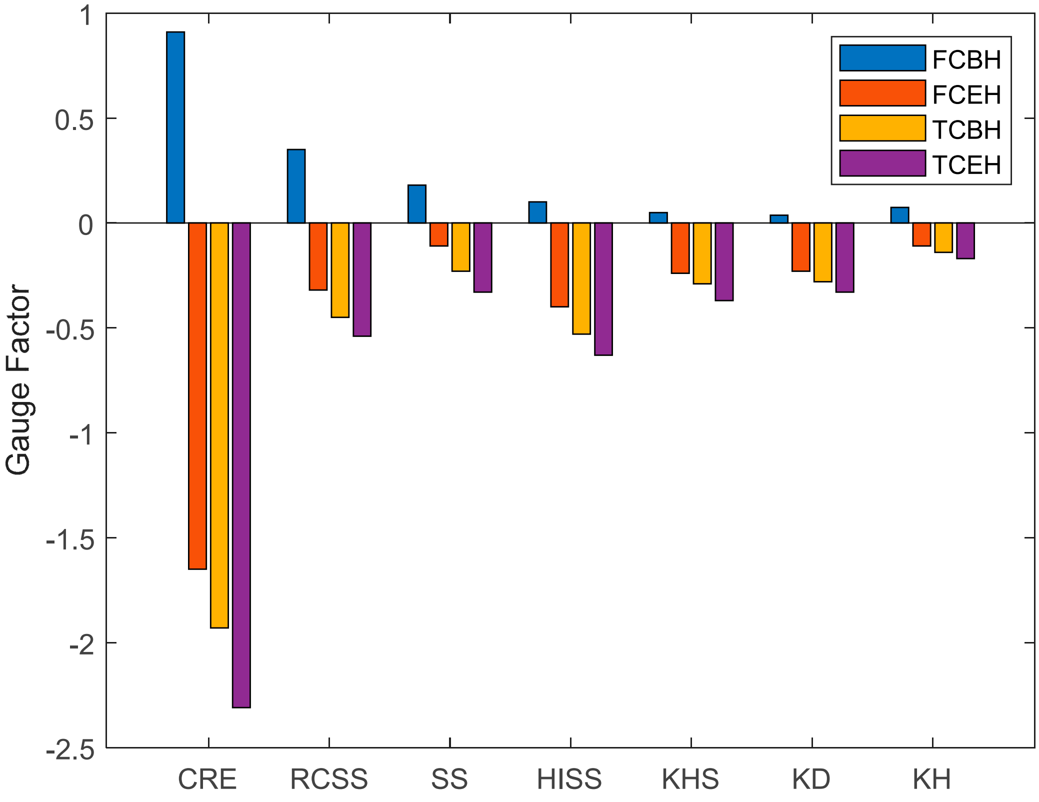

Figure 21. Gauge factor calculated using Equation (1).

4. Discussions

The FEA of structures showed drastic differences between the seven structures used in this study. The CRE demonstrated very low-stress concentrations, mainly because the structure does not have many sharp corners and the stress is more uniformly distributed throughout the structure. It is also observed that the flexibility is very limited in this design, which is approximately in the range of 5.00–10.00 mm.

The serpentine structures have experienced a more complex series of stress concentrations due to the presence of many arches in their design. The stress concentrations were typically larger within the dip of the serpentine structure, which is expected, since the serpentine structures are able to maintain specific geometry based on the "s"-shaped curve. Moreover, the serpentine structures have greater displacement capabilities compared to the CRE. The serpentine structures are capable of elongating up to about 10.00–15.00 mm.

The kirigami structures have shown low stress concentrations, and there are only a few regions with high stress. This is mainly due to the fact that the kirigami structures have rigid body motions during elongation, so the stress concentration thrives in the connection links between body parts of the kirigami structures with rigid body motion. For instance, KHS and KD both have extremely high stress concentrations near the center and edge of the vertical beams. At low-distributed loads, the stress concentration builds up within the central links and at larger loads, the linkages at the edge also began to experience stress concentrations. Both KHS and KD have demonstrated the same stretchability: about 20.00–30.00 mm. Based on the FE results, the KH was the most unique design compared to the other two kirigami structures, as it is capable of maintaining high distributed stress concentrations; however, it also experienced large stress values. This was expected, since the structure was thinly designed, which affected the intersection between the serpentine and dumbbell shape contact point. Despite experiencing high stress values, since the chosen material is highly elastic, the structure is capable of displacing 30.00–60.00 mm, which is 50–100% strain.

Next, all seven structures were tested under cyclic loading to determine their capability for repeated use without damage and the consistency of the results. A ten-cycle loading was chosen to evaluate their performance. As demonstrated in Figure 7, in all seven structures, the resistance decreased every cycle after reaching the maximum. On closer inspection, the first cycle shows an increase in resistance with elongation, which is expected; however, throughout the rest of the test, the resistance displays behavior in opposition to expectations, resulting in a negative gauge factor. Previously, a negative gauge factor or decrease in resistance under tension in polymer nanocomposite was reported by Shui and Chung [24]. They attributed this phenomenon to the increase in the degree of conductive filament alignment along the stress axis upon tension. Lu et al. [25] also reported the negative gauge factor in skin-mountable strain gauges made of carbon-black-doped poly(dimethylsiloxane) (CB-PDMS) and attributed this phenomenon to Poisson's effect. A negative gauge factor for different polymer nanocomposites was also reported in the literature [26–28]. What has been observed in our experiments can be explained as follows.

The first time each structure stretches, there is a permanent increase in resistance in each sample due to the permanent rearrangement of polymer chains and the relative distance between conductive nanoparticles. Once the load is removed from each sample, initially, the resistance decreases as the gaps between conductive nanoparticles decrease, but then starts increasing to a higher value than the original resistance. After the load is completely removed from the sample, both the structure and polymer nanocomposite relax to a configuration that has higher resistance compared to the original unstretched shape.

During the cyclic loading, the magnitude of the gauge factor increases until it converges to a constant value under steady-state conditions. Disregarding the first cycle, similar behavior is observed in the second to tenth cycles, where the resistance decreases significantly then increases slightly or reaches constant resistance before returning to the initial state. Looking closely at the structural deformation, there might be another possible explanation for the s-shaped plot. For example, the kirigami structures have some regions that undergo rigid body motion more significantly than deformation, which can significantly affect the path of electrons through the structures. This type of structural behavior can be seen across all designs under smaller loads. By carefully examining a video recording of the deformation process for all the structures, it is observed that all linkages and connections of the structures initially rotate or tend to straighten out before experiencing any longitudinal or lateral deformation, which may explain the decrease and the following sudden increase in resistance in the middle of elongation.

Figure 19 represents the change in resistance by strain; it is observed that the change in resistance decreases quickly through the first to tenth cycles. Figure 20 presents the initial resistance for the corresponding cycle and Figure 21 presents the gauge factors of the first and last cycles. With the explanations provided regarding the molecule chains' separation and structural opposition to deformation, the structures will continue to provide more negative resistance until an equilibrium state is reached. This becomes more evident during the first cycle, since the gauge factor change between the First Cyclic Before Halfway (FCBH) and First Cyclic End of Halfway (FCEH) is far greater than the change between the Tenth Cyclic Before Halfway (TCBH) and Tenth Cyclic End of Halfway (TCEH), showing that the gauge factor is slowly reaching steady state.

Different structures can be used for different applications, since each structure has its unique elastic limit. Only considering the TCEH region, the structures can be categorized, which is explained next. The CRE has the largest gauge factor of -2.3, meaning that the structure has the greatest negative change in resistance per unit strain. Contrary to the gauge factor performance, the elastic limit, which represents the stretchability, is 10.00 mm for this structure; therefore, the CRE would be ideal for testing small strains. It is also observed that RCSS and HISS have very similar gauge factors of around -0.6. Additionally, SS, KHS, and KD have shown similar gauge factors of -0.35; however, the structures do not have the same elastic limits. The gauge factors of RCSS, HISS, SS, KHS, and KD are significantly smaller than CRE; however, these structures are more stretchable compared to the CRE and can be used for different applications. Finally, the gauge factor of the KH is -0.17, which means this structure shows a very small change in resistance per elongation. Although the change in resistance may be small in this structure, its design allows for a 60.00 mm elastic limit, which is 500% greater than CRE. It is concluded that with the selected filament, the gauge factor is inversely proportional to the stretchability of the structures.

5. Conclusions

In this paper, we studied the electromechanical behavior of seven different structures 3D printed using piezoresistive flexible filament. These structures were selected from the three most common categories for stretchable sensors, namely, serpentine, auxetic, and kirigami. The cyclic tensile tests were conducted on these structures to evaluate their mechanical and electrical performance as stretchable sensors. The results indicated that Curved Re-Entrant (CRE) has the highest sensitivity but the lowest stretchability. When stretchability is the most important factor, Kirigami-based designs perform better while their sensitivity is low. The serpentine shape designs are in between having good stretchability and high sensitivity, with Reduced Curve Serpentine Shape (RCSS) possessing better sensitivity. In the end, obtaining insight from the performance of these structures will help us to come up with a better design in the future.

Author Contributions: Conceptualization, A.E., methodology, E.K.; software, E.K.; validation, E.K.; formal analysis, E.K. and A.E.; investigation, A.E.; resources, S.K. and A.E.; data curation, E.K. and A.E.; writing—original draft preparation, E.K.; writing—review and editing, S.K. and A.E.; visualization, E.K. and A.E.; supervision, A.E.; project administration, A.E.; funding acquisition, S.K. and A.E. All authors have read and agreed to the published version of the manuscript.

Funding: This research was partially funded by NSF-REU program: Multidisciplinary Research Experience in Advance Manufacturing for Undergraduates (Award Number: 2051066).

Data Availability Statement: The raw data are available from the authors upon reasonable request.

Conflicts of Interest: The authors declare no conflict of interest.

Abbreviations

CRE	Curved Re-Entrant
FCBH	First Cycle Before Halfway
FCEH	First Cycle End of Halfway
FDM	Fused Deposition Modeling
HISS	Hourglass Inspired Serpentine Shape
KD	Kirigami Dumbbell
KH	Kirigami Hybrid
KHS	Kirigami H-Shape
RCSS	Reduced Curve Serpentine Shape
SS	Serpentine Shape
TCBH	Tenth Cycle Before Halfway
TCEH	Tenth Cycle End of Halfway
TPU	Thermoplastic Polyurethane

References

1. Liu, H.; Wang, L.; Lin, G.; Feng, Y. Recent progress in the fabrication of flexible materials for wearable sensors. *Biomater. Sci.* **2022**, *10*, 614–632. [CrossRef] [PubMed]
2. Zhang, H.; He, R.; Niu, Y.; Han, F.; Li, J.; Zhang, X.; Xu, F. Graphene-enabled wearable sensors for healthcare monitoring. *Biosens. Bioelectron.* **2022**, *197*, 113777. [CrossRef] [PubMed]
3. Sng, C.M.N.; Wee, L.M.C.; Tang, K.C.; Lee, K.C.J.; Wu, Q.H.; Yeo, J.C.; Bhagat, A.A.S. Wearable Soft Microtube Sensors for Quantitative Home-Based Erectile Dysfunction Monitoring. *Sensors* **2022**, *22*, 9344. [CrossRef] [PubMed]
4. Tang, X.; Yang, W.; Yin, S.; Tai, G.; Su, M.; Yang, J.; Shi, H.; Wei, D.; Yang, J. Controllable graphene wrinkle for a high-performance flexible pressure sensor. *ACS Appl. Mater. Interfaces* **2021**, *13*, 20448–20458. [CrossRef]
5. Hopkins, M.; Vaidyanathan, R.; Mcgregor, A.H. Examination of the performance characteristics of velostat as an in-socket pressure sensor. *IEEE Sens. J.* **2020**, *20*, 6992–7000. [CrossRef]
6. Zhu, Y.; Li, X.; Zhao, Z.; Liang, Y.; Wang, L.; Liu, Y. Highly Stretchable, Transparent and Adhesive Ionogel Based on Chitosan-Poly (acrylic acid) Double Networks for Flexible Strain Sensors. *Gels* **2022**, *8*, 797. [CrossRef]
7. Yang, D.; Yang, W.; Li, L.; Zhou, K.; Hao, M.; Feng, X.; Zhang, T.; Liu, Y. Highly Sensitive Microstructure-Based Flexible Pressure Sensor for Quantitative Evaluation of Motor Function Recovery after Spinal Cord Injury. *Sensors* **2019**, *19*, 4673. [CrossRef]
8. Sundaram, S.; Kellnhofer, P.; Li, Y.; Zhu, J.-Y.; Torralba, A.; Matusik, W. Learning the signatures of the human grasp using a scalable tactile glove. *Nature* **2019**, *569*, 698–702. [CrossRef]
9. Oh, D.; Seo, J.; Kim, H.G.; Ryu, C.; Bang, S.-W.; Park, S.; Kim, H.J. Multi-height micropyramids based pressure sensor with tunable sensing properties for robotics and step tracking applications. *Micro Nano Syst. Lett.* **2022**, *10*, 1–7. [CrossRef]
10. Zhong, M.; Zhang, L.; Liu, X.; Zhou, Y.; Zhang, M.; Wang, Y.; Yang, L.; Wei, D. Wide linear range and highly sensitive flexible pressure sensor based on multistage sensing process for health monitoring and human-machine interfaces. *Chem. Eng. J.* **2021**, *412*, 128649. [CrossRef]
11. Salo, T.; Di Vito, D.; Halme, A.; Vanhala, J. Electromechanical Properties of 3D-Printed Stretchable Carbon Fiber Composites. *Micromachines* **2022**, *13*, 1732. [CrossRef] [PubMed]
12. Tang, Z.; Jia, S.; Zhou, C.; Li, B. 3D printing of highly sensitive and large-measurement-range flexible pressure sensors with a positive piezoresistive effect. *ACS Appl. Mater. Interfaces* **2020**, *12*, 28669–28680. [CrossRef] [PubMed]
13. Verma, P.; Ubaid, J.; Varadarajan, K.M.; Wardle, B.L.; Kumar, S. Synthesis and Characterization of Carbon Nanotube-Doped Thermoplastic Nanocomposites for the Additive Manufacturing of Self-Sensing Piezoresistive Materials. *ACS Appl. Mater. Interfaces* **2022**, *14*, 8361–8372. [CrossRef] [PubMed]
14. Lanzolla, A.M.L.; Attivissimo, F.; Percoco, G.; Ragolia, M.A.; Stano, G.; Di Nisio, A. Additive manufacturing for sensors: Piezoresistive strain gauge with temperature compensation. *Appl. Sci.* **2022**, *12*, 8607. [CrossRef]
15. Widlund, T.; Yang, S.; Hsu, Y.-Y.; Lu, N. Stretchability and compliance of freestanding serpentine-shaped ribbons. *Int. J. Solids Struct.* **2014**, *51*, 4026–4037. [CrossRef]
16. Sim, K.; Li, Y.; Song, J.; Yu, C. Biaxially stretchable ultrathin Si enabled by serpentine structures on prestrained elastomers. *Adv. Mater. Technol.* **2019**, *4*, 1800489. [CrossRef]
17. Meena, K.; Singamneni, S. A new auxetic structure with significantly reduced stress concentration effects. *Mater. Des.* **2019**, *173*, 107779. [CrossRef]
18. Jiang, Y.; Liu, Z.; Matsuhisa, N.; Qi, D.; Leow, W.R.; Yang, H.; Yu, J.; Chen, G.; Liu, Y.; Wan, C. Auxetic mechanical metamaterials to enhance sensitivity of stretchable strain sensors. *Adv. Mater.* **2018**, *30*, 1706589. [CrossRef]

19. Zhou, X.; Parida, K.; Halevi, O.; Liu, Y.; Xiong, J.; Magdassi, S.; Lee, P.S. All 3D-printed stretchable piezoelectric nanogenerator with non-protruding kirigami structure. *Nano Energy* **2020**, *72*, 104676. [CrossRef]
20. Lee, H.C.; Hsieh, E.Y.; Yong, K.; Nam, S. Multiaxially-stretchable kirigami-patterned mesh design for graphene sensor devices. *Nano Res.* **2020**, *13*, 1406–1412. [CrossRef]
21. Wang, L.; Chiang, W.-H.; Loh, K.J. Topological design of strain sensing nanocomposites. *Sci. Rep.* **2022**, *12*, 9179. [CrossRef] [PubMed]
22. Taherkhani, B.; Azizkhani, M.B.; Kadkhodapour, J.; Anaraki, A.P.; Rastgordani, S. Highly sensitive, piezoresistive, silicone/carbon fiber-based auxetic sensor for low strain values. *Sens. Actuators A Phys.* **2020**, *305*, 111939. [CrossRef]
23. Liu, H.; Kollosche, M.; Yan, J.; Zellner, E.M.; Bentil, S.A.; Rivero, I.V.; Wiersema, C.; Laflamme, S. Numerical investigation of auxetic textured soft strain gauge for monitoring animal skin. *Sensors* **2020**, *20*, 4185. [CrossRef] [PubMed]
24. Shui, X.; Chung, D. A new electromechanical effect in discontinuous-filament elastomer-matrix composites. *Smart Mater. Struct.* **1997**, *6*, 102. [CrossRef]
25. Lu, N.; Lu, C.; Yang, S.; Rogers, J. Highly sensitive skin-mountable strain gauges based entirely on elastomers. *Adv. Funct. Mater.* **2012**, *22*, 4044–4050. [CrossRef]
26. Johnson, O.K.; Kaschner, G.C.; Mason, T.A.; Fullwood, D.T.; Hansen, G. Optimization of nickel nanocomposite for large strain sensing applications. *Sens. Actuators A Phys.* **2011**, *166*, 40–47. [CrossRef]
27. Li, S.; Park, J.G.; Wang, S.; Liang, R.; Zhang, C.; Wang, B. Working mechanisms of strain sensors utilizing aligned carbon nanotube network and aerosol jet printed electrodes. *Carbon* **2014**, *73*, 303–309. [CrossRef]
28. Yan, Y.; Sencadas, V.; Zhang, J.; Zu, G.; Wei, D.; Jiang, Z. Processing, characterisation and electromechanical behaviour of elastomeric multiwall carbon nanotubes-poly (glycerol sebacate) nanocomposites for piezoresistive sensors applications. *Compos. Sci. Technol.* **2017**, *142*, 163–170. [CrossRef]